Supporting Information

Synergistic Effect Promoting Proton Transport in Metal-Organic Framework Aerogels

Xiao-Min Li,*[a] Junchao Jia,[a] Dongbo Liu,[a] Aziz Bakhtiyarovich Ibragimov,[b] Junkuo Gao*[a]

[a] China-Uzbekistan Joint Laboratory on Advanced Porous Materials, School of Materials Science and Engineering, Zhejiang Sci-Tech University, Hangzhou 310018, P. R. China.

[b] Institute of General and Inorganic Chemistry, Uzbekistan Academy of Sciences, Tashkent 100170, Uzbekistan

*Corresponding Author

Email address:

lixm@zstu.edu.cn (X.-M. Li);

jkgao@zstu.edu.cn (J. Gao)

EXPERIMENTAL SECTION

Material. Zirconium(IV) chloride ($ZrCl_4$), polyvinyl alcohol and formic acid (HCOOH) were obtained from Macklin. 1, 3, 5-Benzenetricarboxylic acid (H_3BTC) was purchased from Energy Chemical. 1, 2, 4-benzenetricarboxylic acid (H_3BTEC) was purchased from Aladdin. Ethanol absolute (CH_3CH_2OH) was purchased from Sinopharm Chemical Reagent Co. Ltd. All these chemicals were used without further purification.

Synthesis of UiO-66-COOH. The MOF was synthesized by the previous literature with some changes.[1] 1.86 g $ZrCl_4$ and 1.7 g H_3BTC were dissolved in 35 mL H_2O. The resulting solution was subsequently subjected to heating in an oven at 100 ℃ for 24 h. Following the heating period, the solution was allowed to cool to room temperature, after which the solid was collected and washed with H_2O and ethanol absolute, each performed 3 times. Finally, the products were centrifuged and dried on a vacuum oven at 80 °C.

Synthesis of UiO-66-2COOH. The MOF was synthesized by the previous literature with some changes.[2] 233 mg $ZrCl_4$ and 242 mg H_3BTEC were dissolved in a mixed solvent comprising 14 mL formic acid and 6 mL H_2O. The resulting solution was subsequently heated in an oven at 120 ℃ for 3 h. Following the heating period, the solution was allowed to cool to room temperature, after which the solid precipitate was collected and washed with H_2O and ethanol absolute, each performed 3 times. Finally, the products were centrifuged and dried in a vacuum oven at 80 °C.

Synthesis of UiO-66-COOH aerogel. Polyvinyl alcohol (PVA) was dissolved in deionized water at a mass/volume ratio of 1:10 at 85 ℃. Subsequently, a mixture consisting of UiO-66-COOH (1g) and PVA solution (3.15 mL) was introduced into deionized water (1.5 mL), and subjected to high-speed stirring at 1000 r min^{-1} for 2 hours. Following the stirring process, the resultant product underwent ultrasonic treatment to facilitate defoaming, after which it was transferred into an acrylic mold. This mold was then immersed in an ice-ethanol bath maintained at -80 ℃ and subjected to freeze-dried for 48 hours.

Synthesis of UiO-66-2COOH aerogel. This preparation procedure aligns with the

aforementioned process, with the exception that UiO-66-COOH is substituted with UiO-66-2COOH.

Synthesis of PVA aerogel. A PVA solution (3.15 mL) was combined with deionized water (1.5 mL) and subjected to high-speed stirring at 1000 r min^{-1} for 2 hours. Following the stirring process, the resultant mixture underwent ultrasonic treatment to eliminate foam, after which it was transferred into an acrylic mold. The mold was subsequently immersed in an ice-ethanol bath maintained at -80 ℃ and was freeze-dried for 48 hours.

Apparatus. Powder X-ray diffraction data (PXRD) were recorded on a Bruker D8 Advance diffractometer using a graphite-monochromatized Cu Kα (λ = 1.5418 Å) radiation, and the measured parameter included a scan speed of 5° min^{-1} and a scan range of 2θ from 5 to 50°. Thermogravimetric analysis (TGA) was conducted on a NETZSCH TG 209 F1 apparatus with a heating rate of 10 °C min^{-1} from ambient temperature to 900 °C under a N_2 atmosphere. The Brunauer−Emmett−Teller specific areas of the samples were calculated using N_2 adsorption isotherms obtained at 77 K. Scanning electron microscopy (SEM) images and energy-dispersive X-ray spectroscopy (EDX) of the composite materials were performed by the GeminiSEM 500.The Fourier transform infrared (FTIR) data were collected by a Fourier transform infrared spectrometer (Nicolet 5700, Thermo Electron Corp., USA) in the range of 4000−400 cm^{-1}. Compression curves were recorded at room temperature using the instron-5982 instrument. The water contact angle tests were conducted by OCA 15EC contact angle tester of Data Physics Instruments GmbH, Germany.

Proton Conductivity Test. UiO-66-COOH and UiO-66-2COOH were processed into powders utilizing an agate mortar prior to conducting proton conductivity measurements. Subsequently, the powders were compacted into tablets using a tablet press machine, and their thickness was recorded. Gold wire was affixed to both sides of the sample stage employing silver colloid. Furthermore, UiO-66-COOH aerogel and UiO-66-2COOH aerogel were shaped and sized appropriately, and then secured between two gold plates for testing purposes. An electrochemical workstation was employed to evaluate the proton conductivity with an input voltage of 100 mV and a

frequency range spanning from 1 MHz to 1 Hz. The humidity during measurements was maintained between 40 and 98% RH, while the temperature was controlled within the range of 30 to 70 ℃. The bulk proton conductivity (σ/S cm^{-1}) was determined using the following equation (l, the thickness of the tablet; S, πr^2; R, resistance/Ω)

$$\sigma = l / (S \times R) \quad (1)$$

The activation energy (E_a) was calculated by the Arrhenius equation (k_B, Boltzmann constant/eV K^{-1}; T, temperature/K)

$$\sigma T = \sigma_0 \exp(-E_a/k_B T) \quad (2)$$

Cycle-dependent proton conductivity tests: The MOFs aerogels were put at 70 ˚C and 98% RH to measure their resistances, and then were put into environmental conditions to restore to the original state, which is referred to as a cycle.

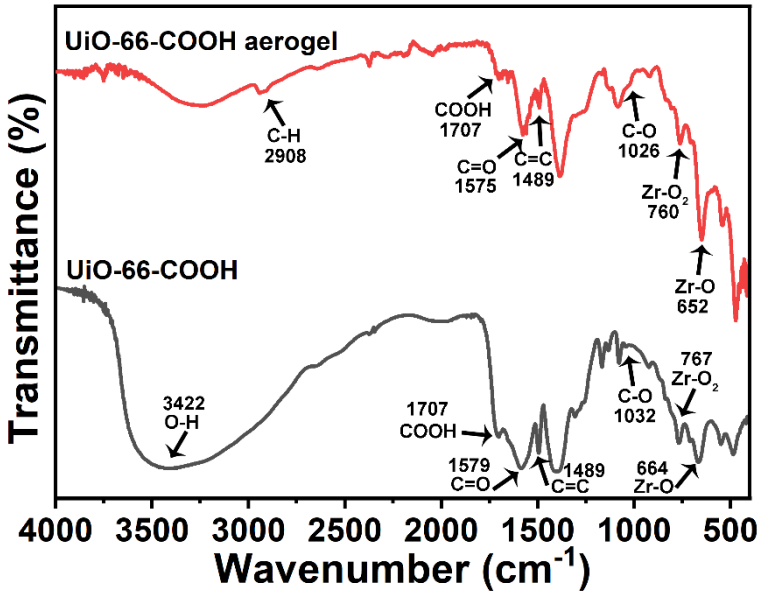

Fig. S1. FT-IR spectra of UiO-66-COOH and UiO-66-COOH aerogel.

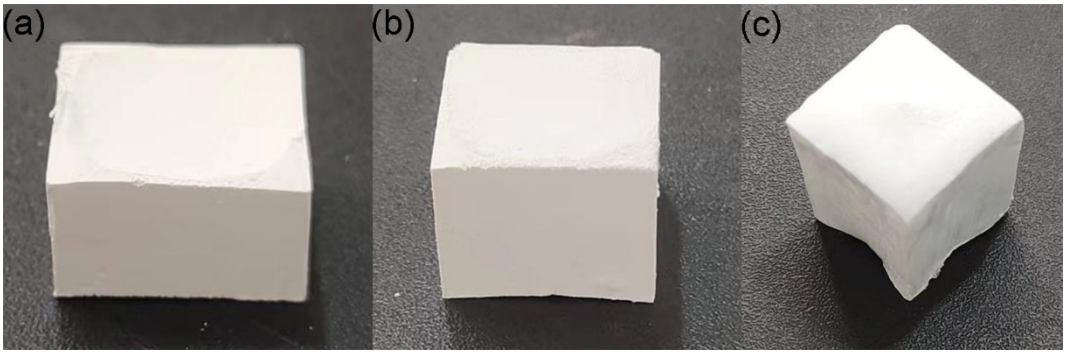

Fig. S2. The digital photographs of (a) UiO-66-COOH aerogel, (b) UiO-66-2COOH

aerogel, and (c) PVA aerogel.

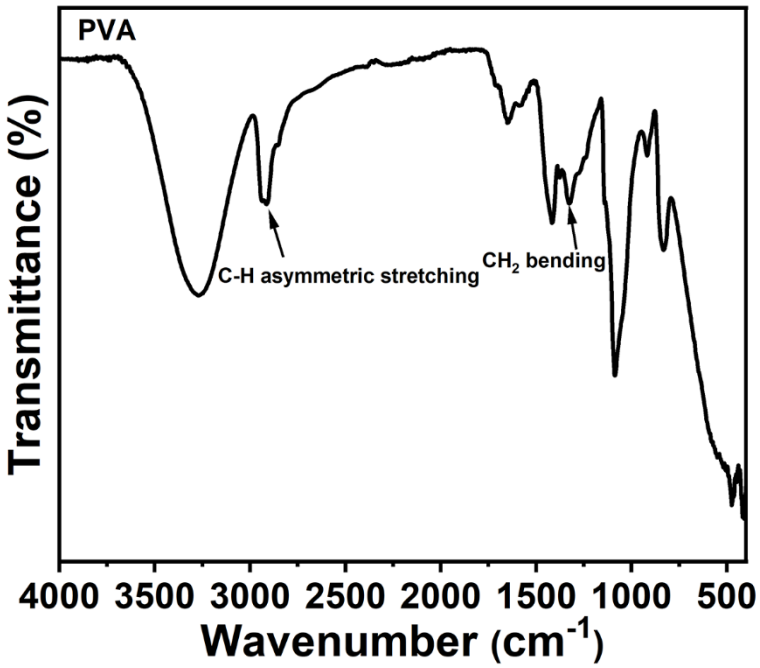

Fig. S3. FT-IR spectrum of PVA.

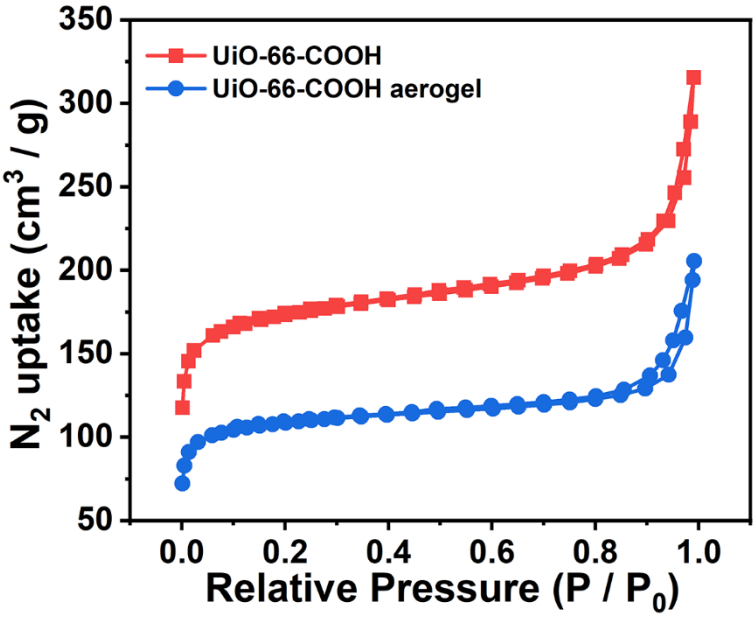

Fig. S4. N_2 adsorption-desorption isotherms of UiO-66-COOH and UiO-66-COOH aerogel.

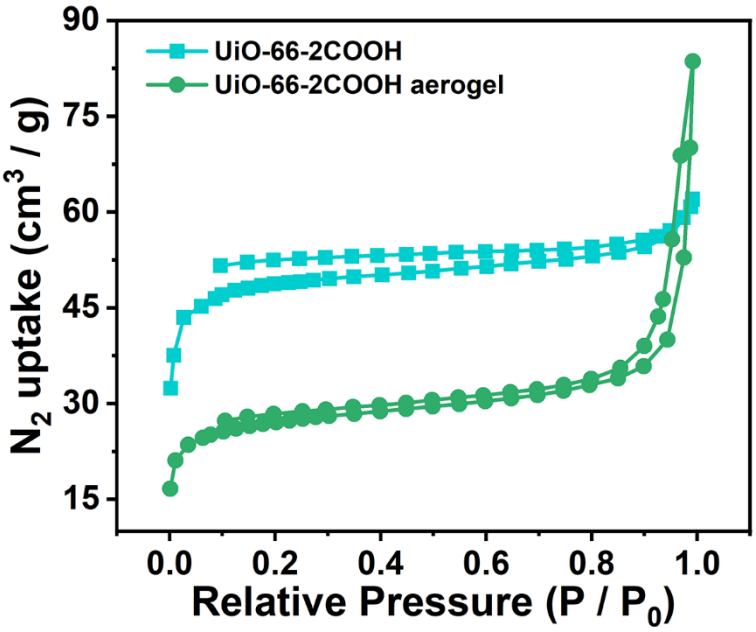

Fig. S5. N_2 adsorption-desorption isotherms of UiO-66-2COOH and UiO-66-2COOH aerogel.

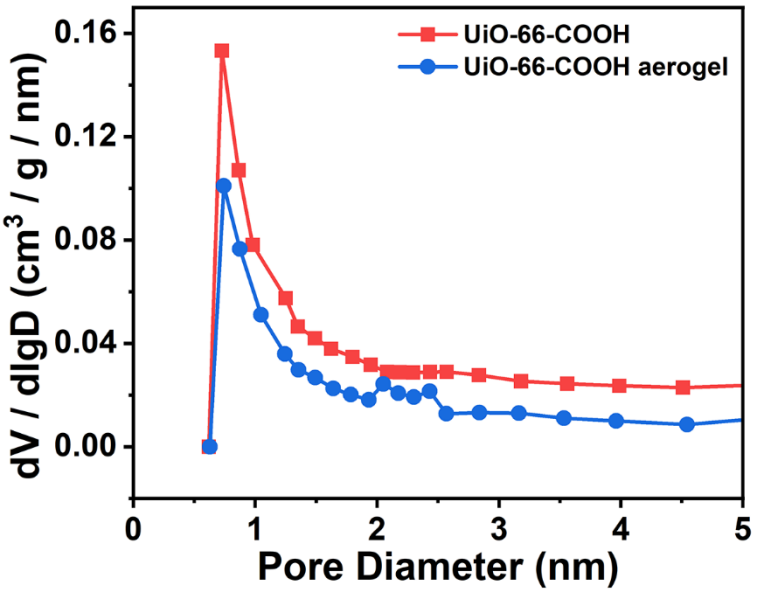

Fig. S6. Pore size distribution curves of UiO-66-COOH and UiO-66-COOH aerogel.

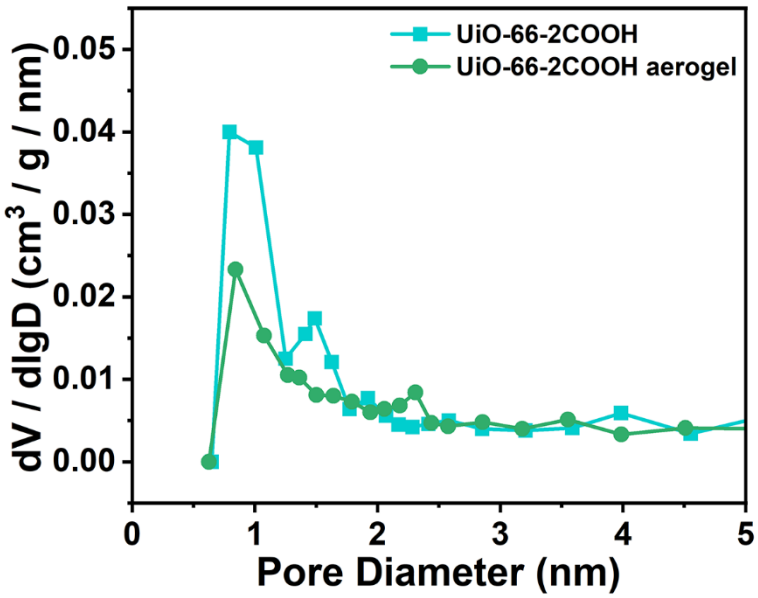

Fig. S7. Pore size distribution curves of UiO-66-2COOH and UiO-66-2COOH aerogel.

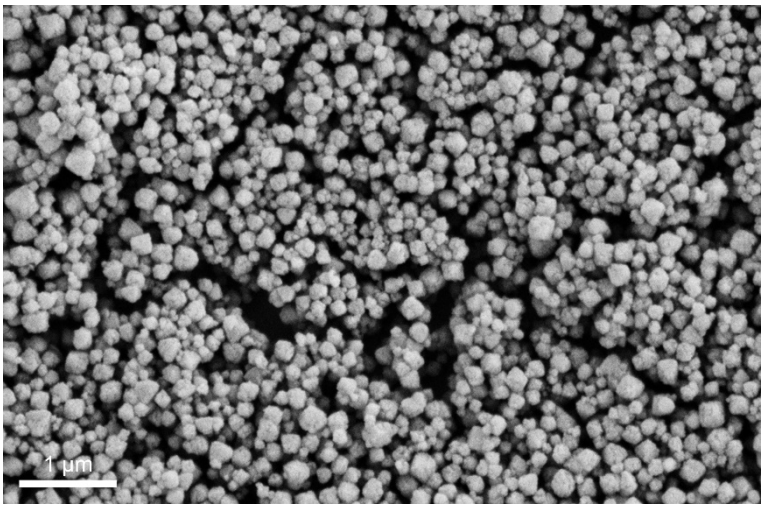

Fig. S8. A typical SEM image of UiO-66-COOH.

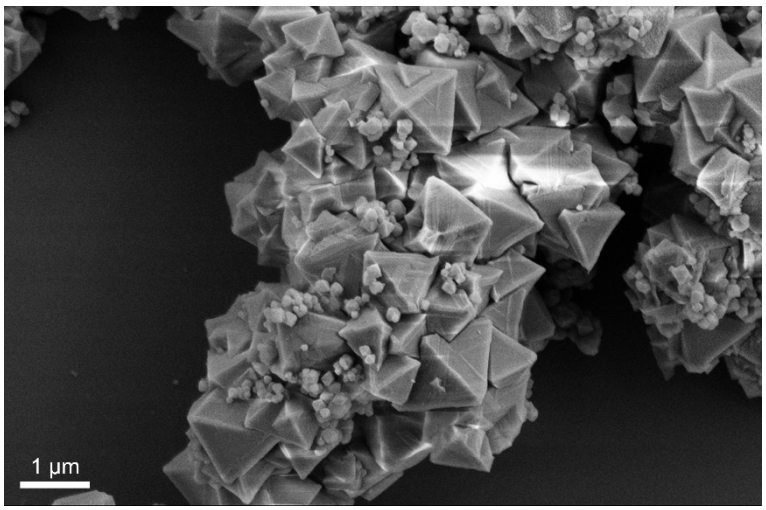

Fig. S9. A typical SEM image of UiO-66-2COOH.

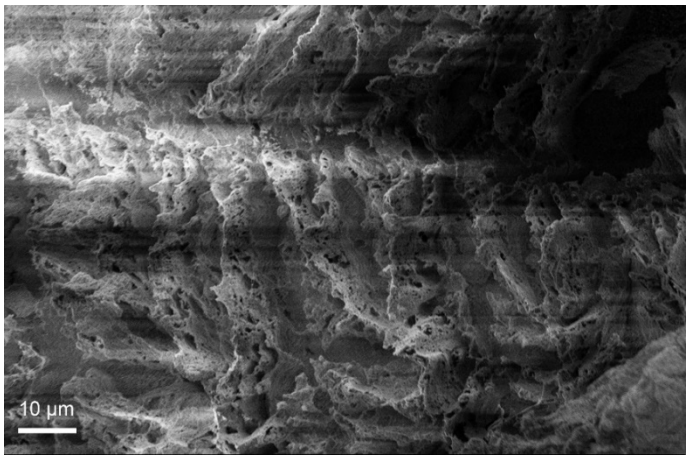

Fig. S10. A typical SEM image of UiO-66-COOH aerogel in the transverse direction.

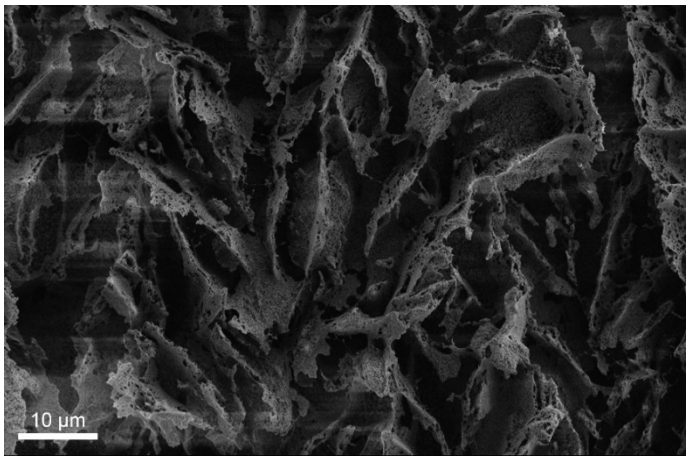

Fig. S11. A typical SEM image of UiO-66-COOH aerogel in the longitudinal direction.

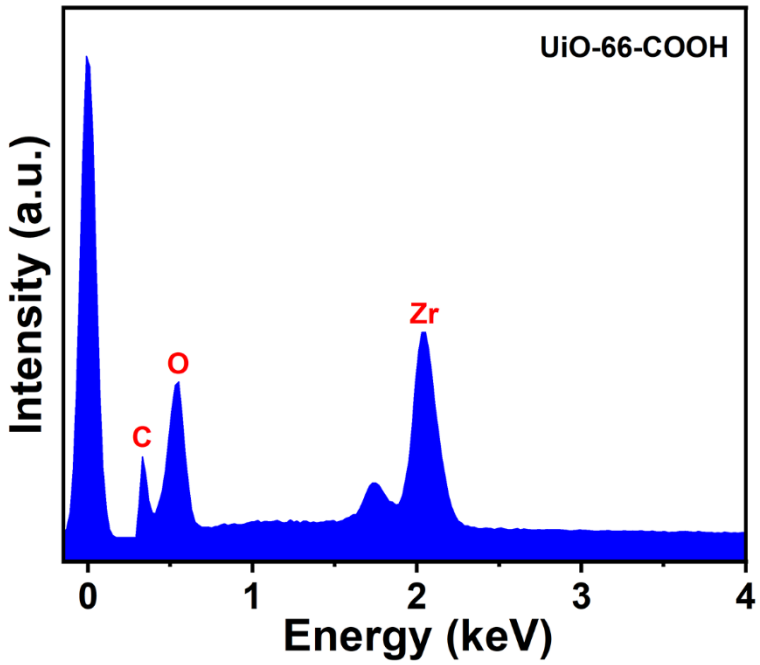

Fig. S12. Energy-dispersive X-ray (EDX) spectrum of UiO-66-COOH.

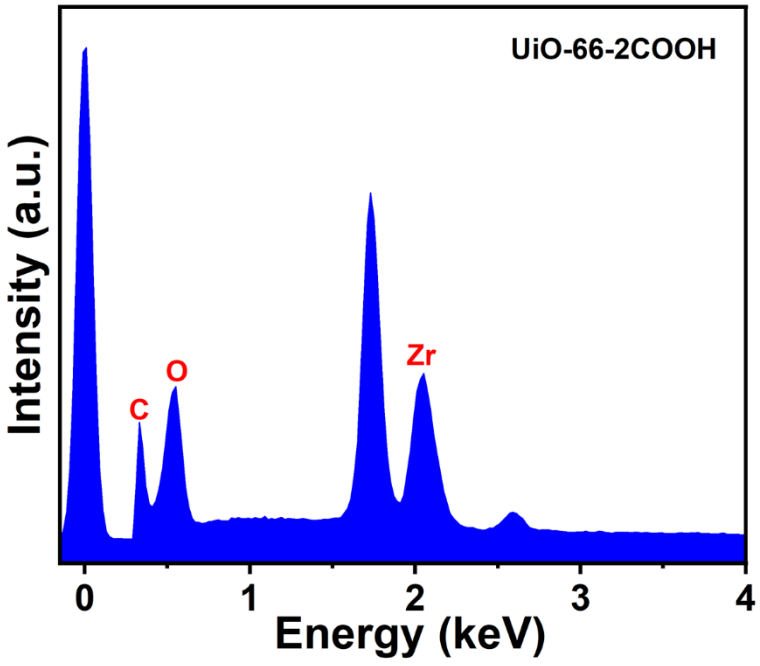

Fig. S13. Energy-dispersive X-ray (EDX) spectrum of UiO-66-2COOH.

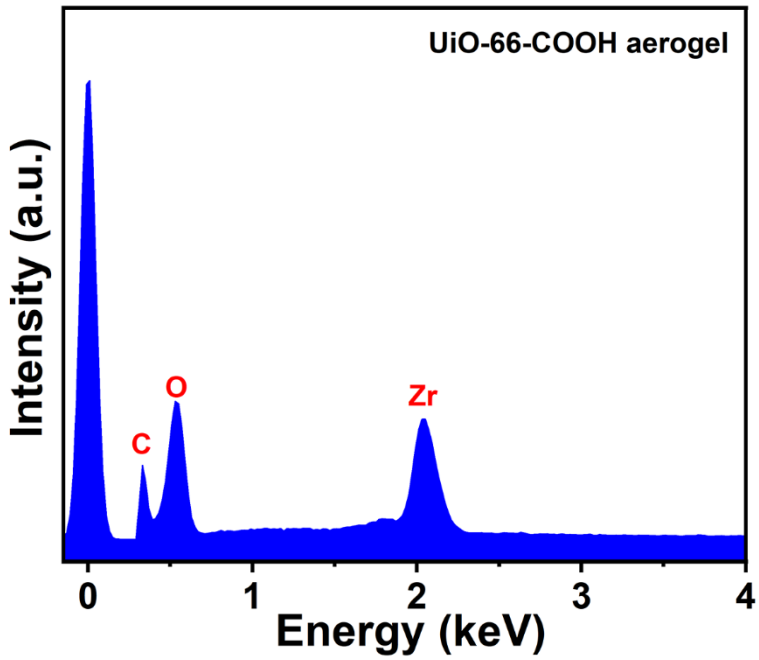

Fig. S14. Energy-dispersive X-ray (EDX) spectrum of UiO-66-COOH aerogel.

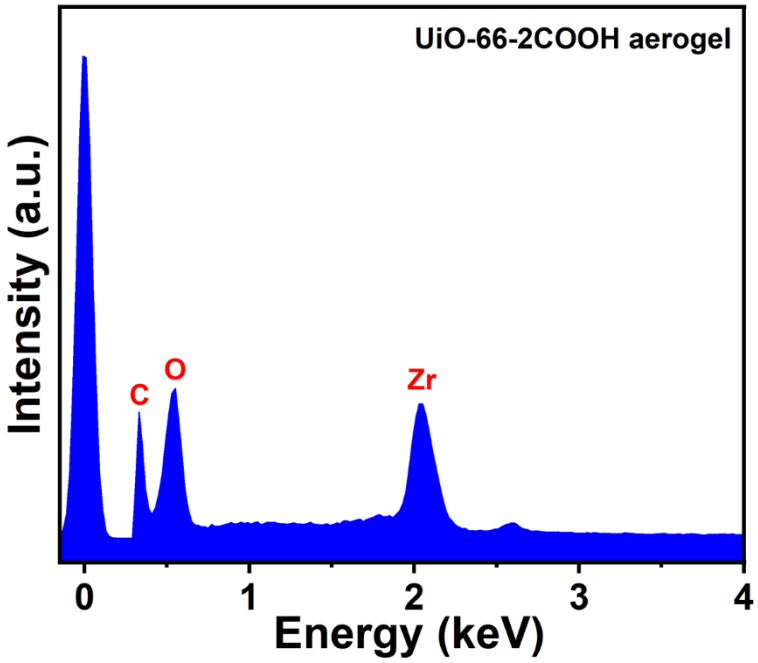

Fig. S15. Energy-dispersive X-ray (EDX) spectrum of UiO-66-2COOH aerogel.

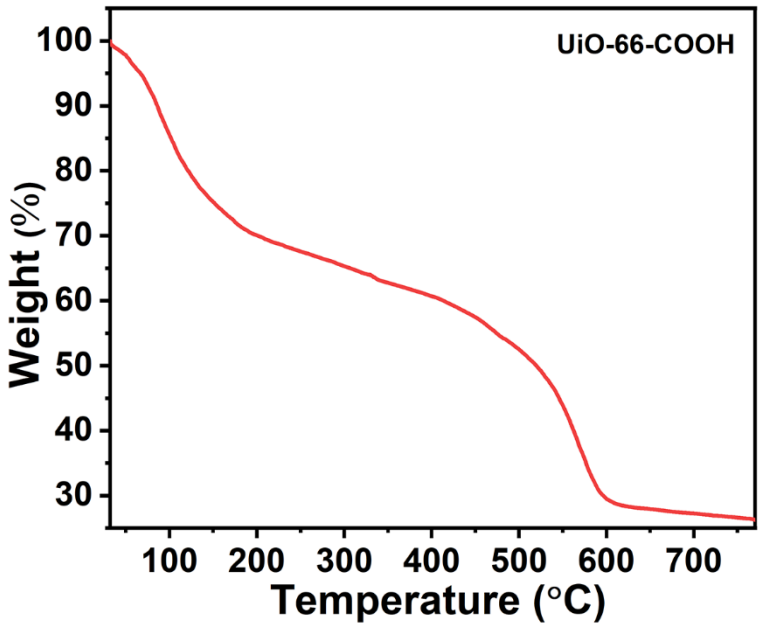

Fig. S16. TGA curve of UiO-66-COOH.

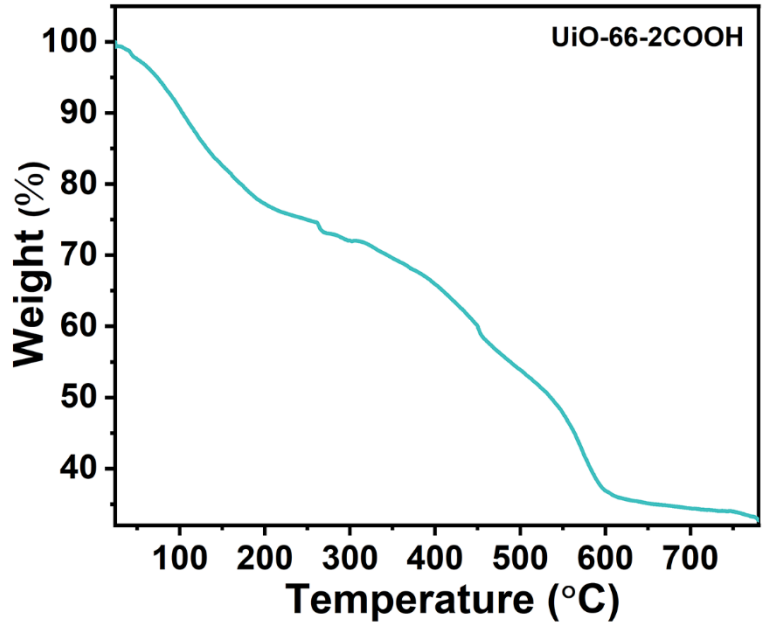

Fig. S17. TGA curve of UiO-66-2COOH.

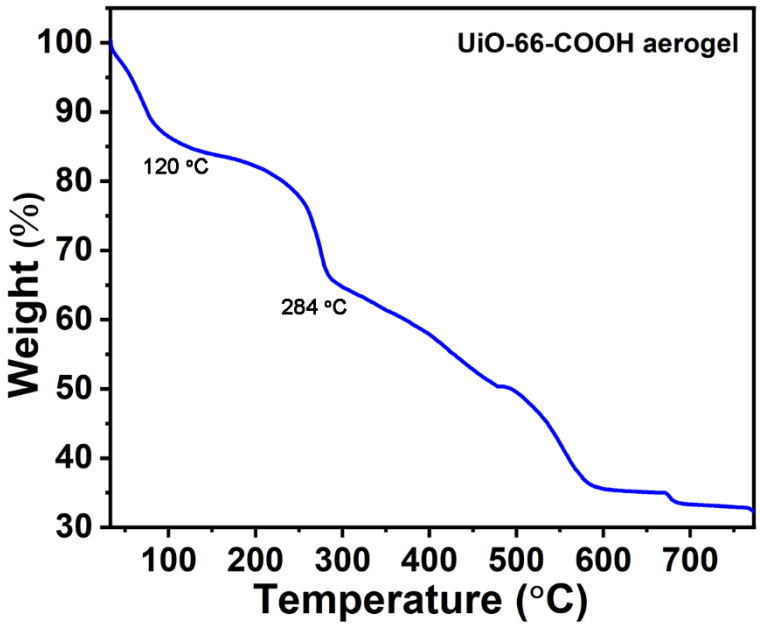

Fig. S18. TGA curve of UiO-66-COOH aerogel.

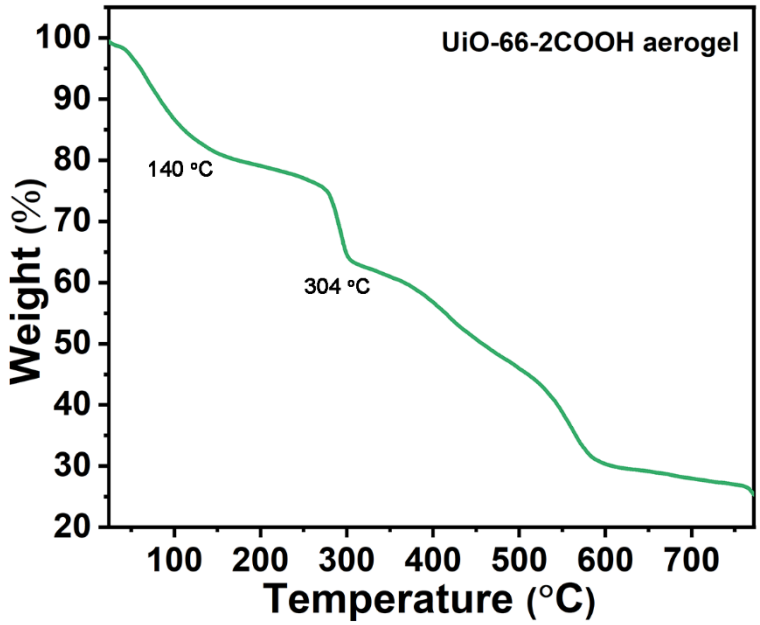

Fig. S19. TGA curve of UiO-66-2COOH aerogel.

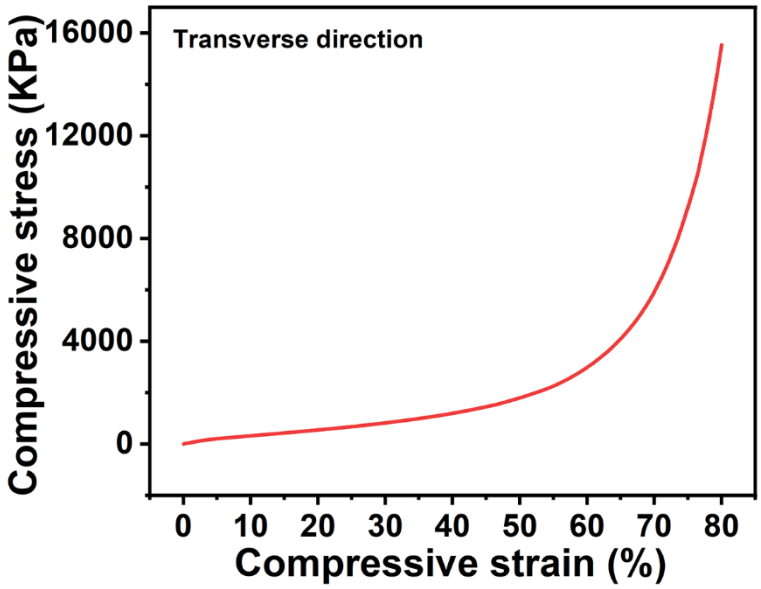

Fig. S20. Compressive stress-strain curve of UiO-66-COOH aerogel at transverse direction.

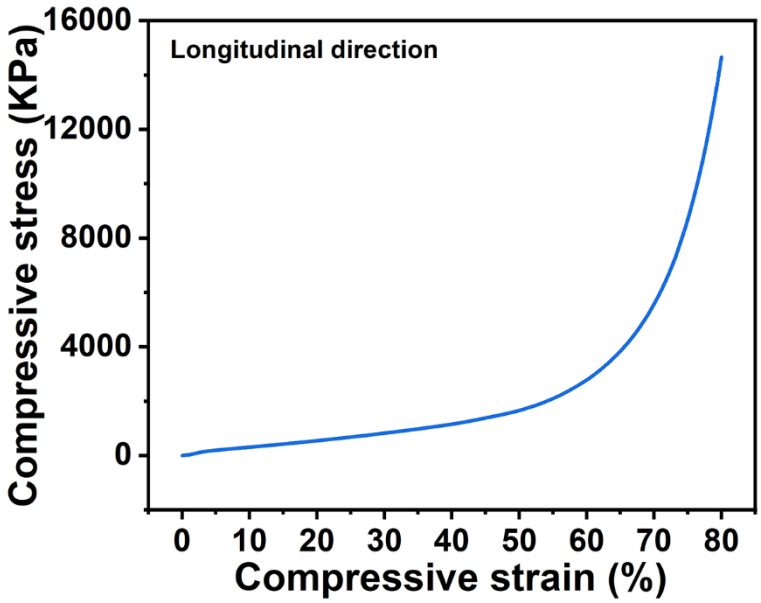

Fig. S21. Compressive stress-strain curve of UiO-66-COOH aerogel at longitudinal direction.

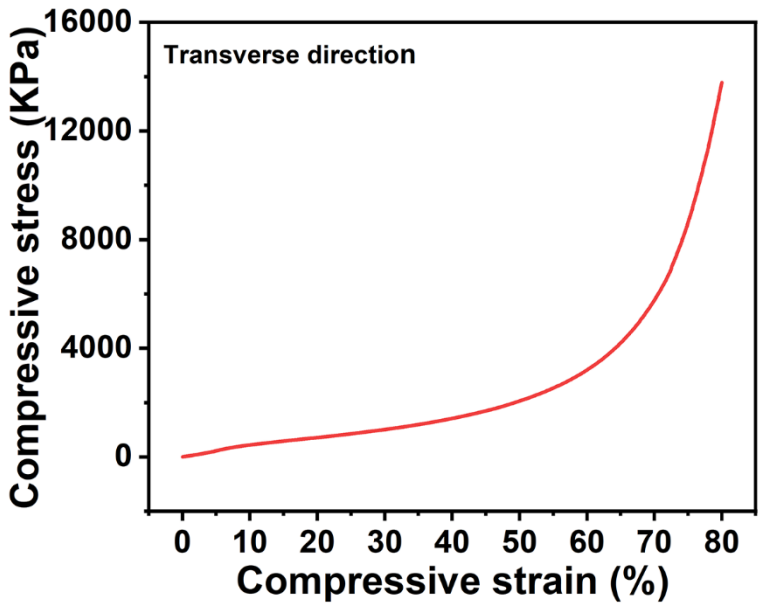

Fig. S22. Compressive stress-strain curve of UiO-66-2COOH aerogel at transverse direction.

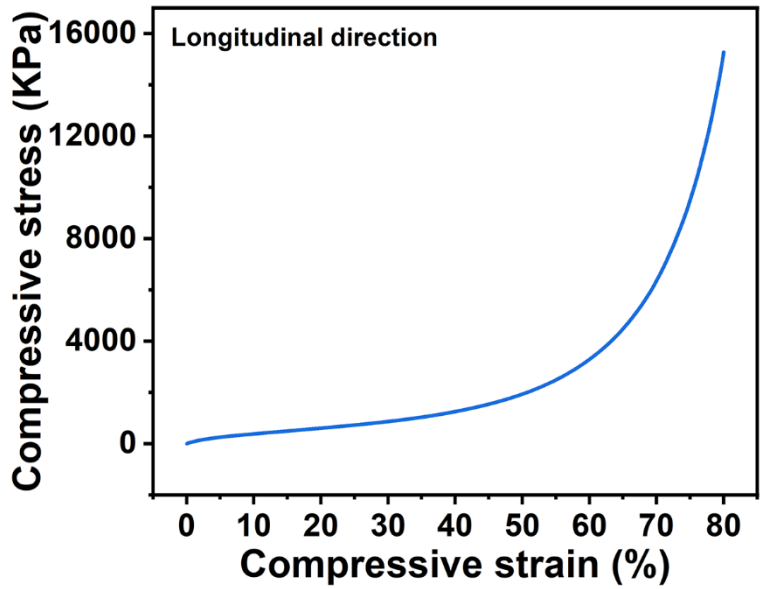

Fig. S23. Compressive stress-strain curve of UiO-66-2COOH aerogel at longitudinal direction.

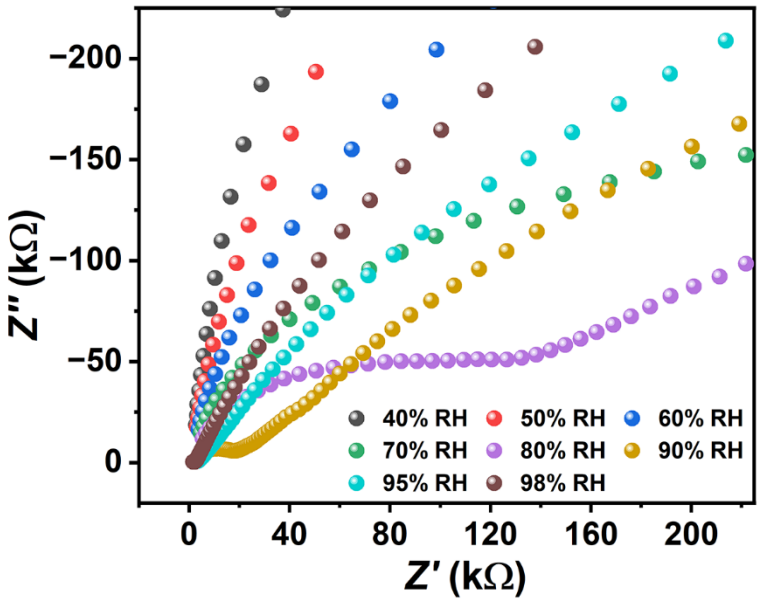

Fig. S24. Nyquist plots of UiO-66-COOH at 30 ℃ and different humidities variation from 40% to 98% RH.

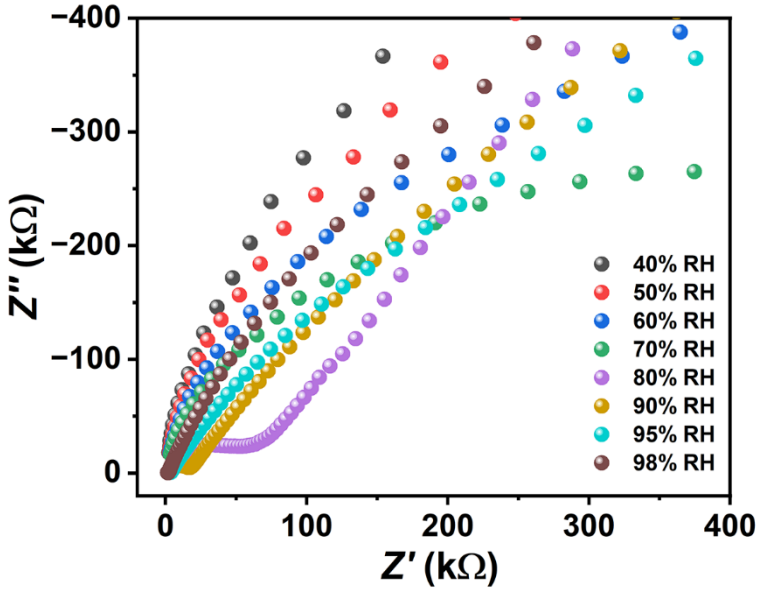

Fig. S25. Nyquist plots of UiO-66-2COOH at 30 ℃ and different humidities variation from 40% to 98% RH.

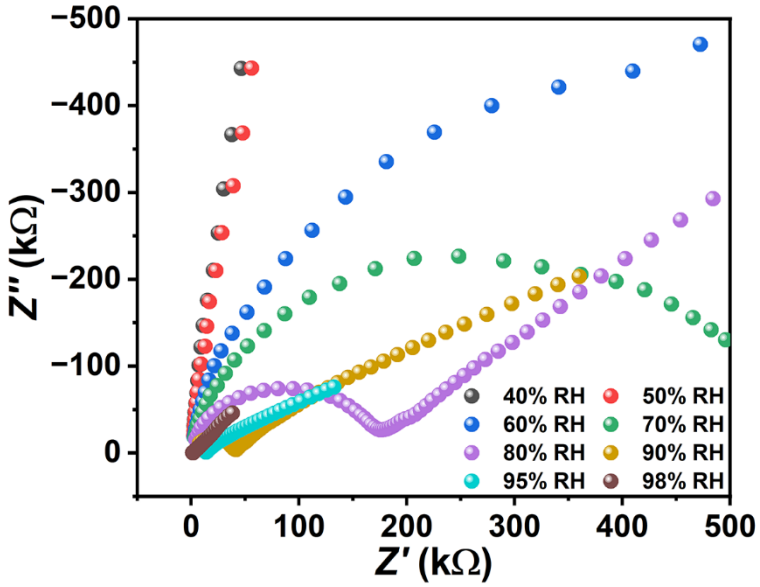

Fig. S26. Nyquist plots of UiO-66-COOH aerogel at 30 ℃ and different humidities variation from 40% to 98% RH.

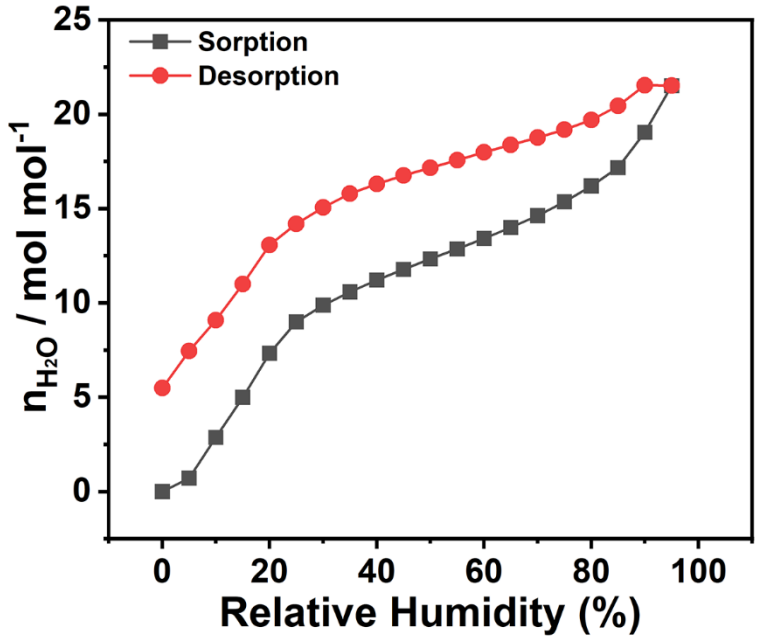

Fig. S27. H_2O adsorption isotherm of UiO-66-COOH aerogel measured at 298 K.

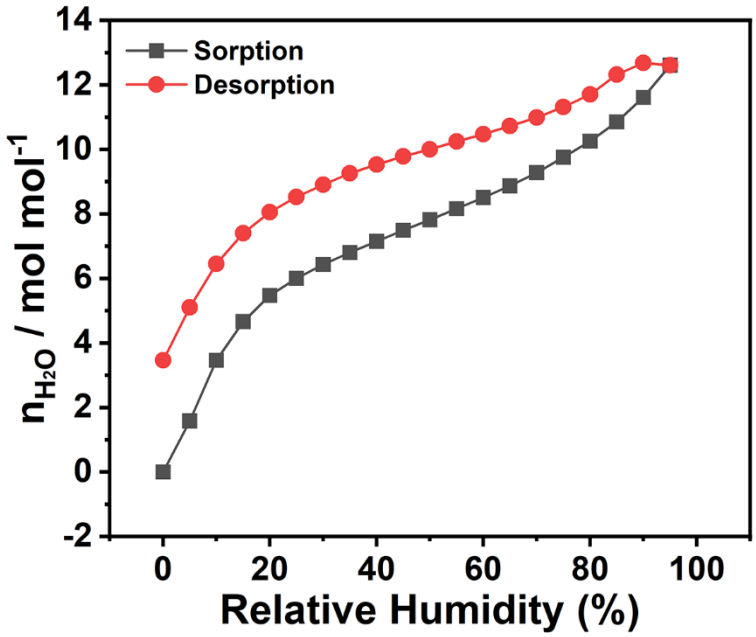

Fig. S28. H_2O adsorption isotherm of UiO-66-2COOH aerogel measured at 298 K.

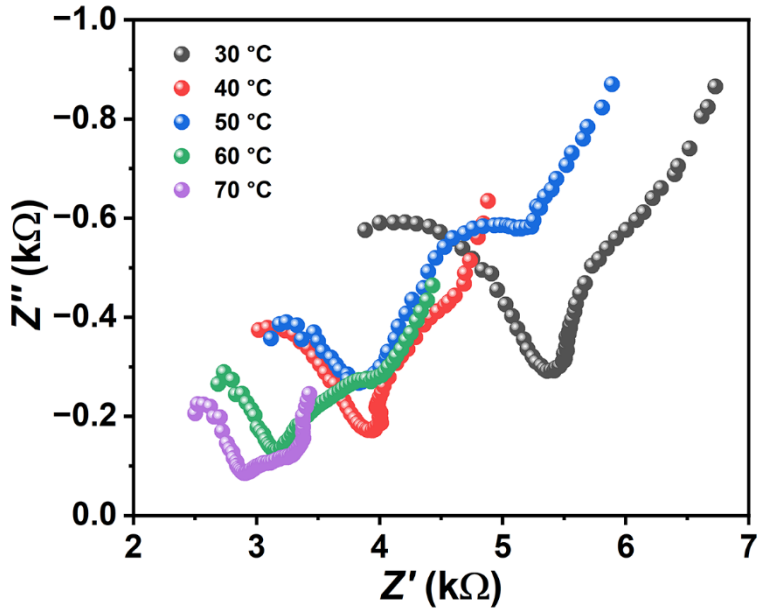

Fig. S29. Nyquist plots of UiO-66-COOH at 98% RH and different temperature variations from 30 to 70 ℃.

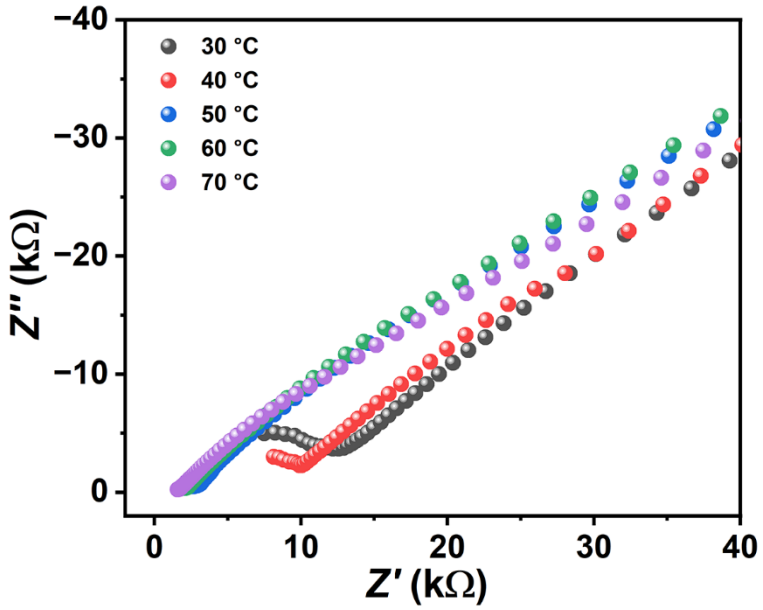

Fig. S30. Nyquist plots of UiO-66-2COOH at 98% RH and different temperature variations from 30 to 70 ℃.

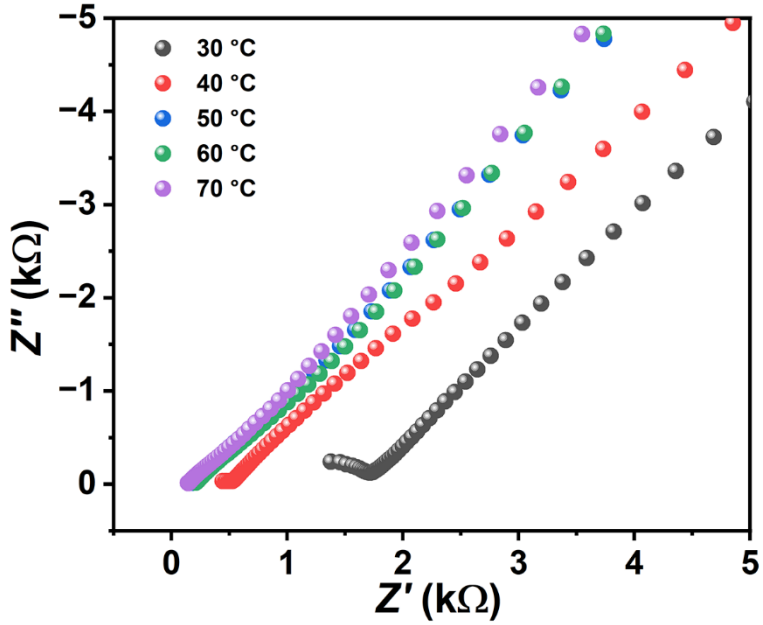

Fig. S31. Nyquist plots of UiO-66-COOH aerogel at 98% RH and different temperature variations from 30 to 70 ℃.

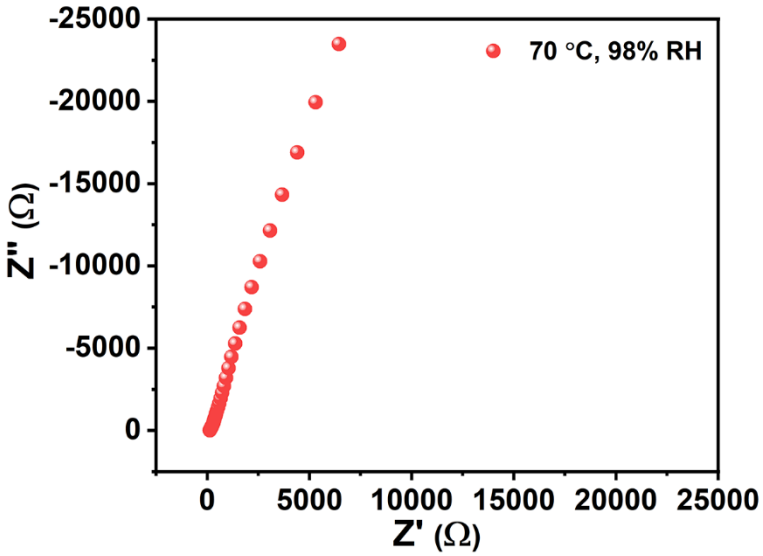

Fig. S32. Nyquist plot of PVA aerogel at 70 ℃ and 98% RH.

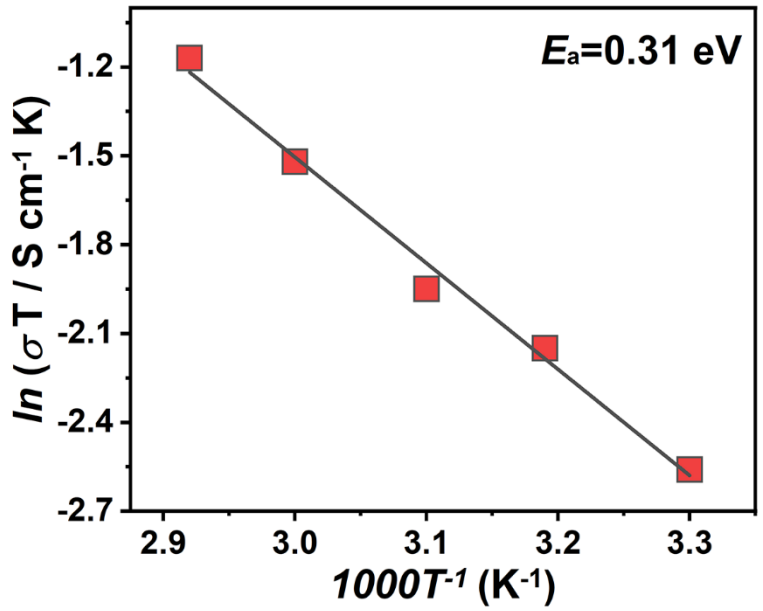

Fig. S33. Arrhenius plot of UiO-66-COOH at 98% RH and the temperature range of 30 to 70 ℃.

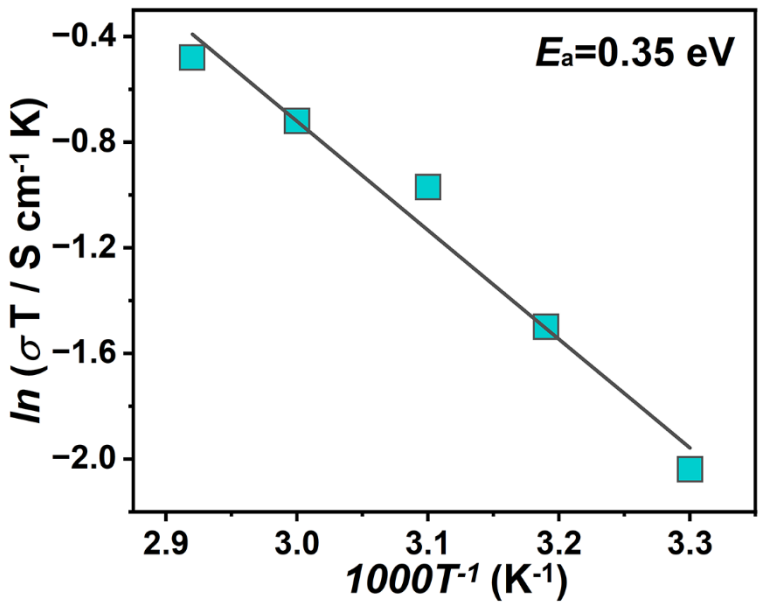

Fig. S34. Arrhenius plot of UiO-66-2COOH at 98% RH and the temperature range of 30 to 70 ℃.

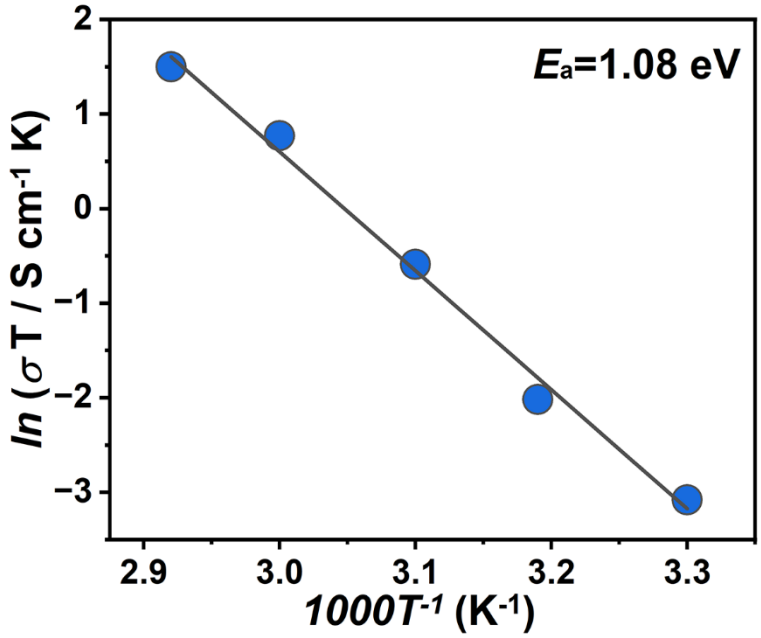

Fig. S35. Arrhenius plot of UiO-66-COOH aerogel at 98% RH and the temperature range of 30 to 70 ℃.

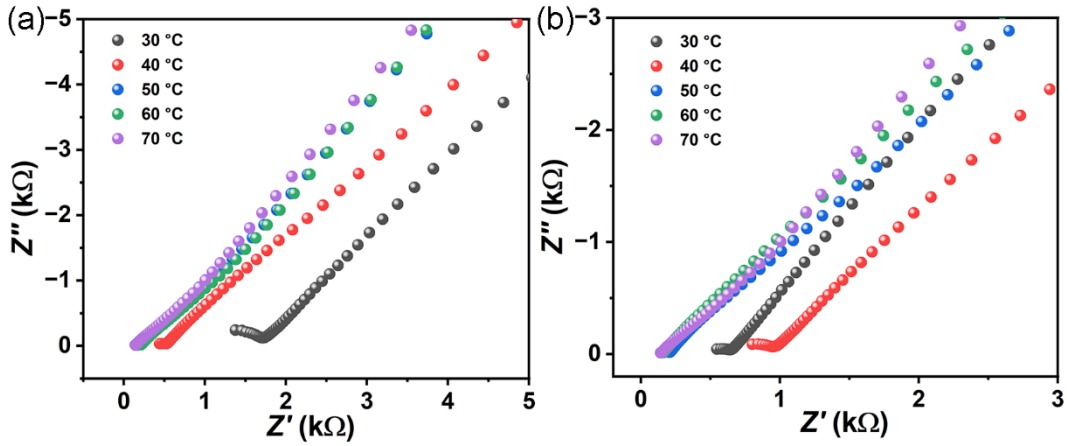

Fig. S36. Nyquist plots for the heating-cooling cycle of UiO-66-COOH aerogel at 98% RH: (a) the heating cycle (30 to 70 ℃); (b) the cooling cycle (70 to 30 ℃).

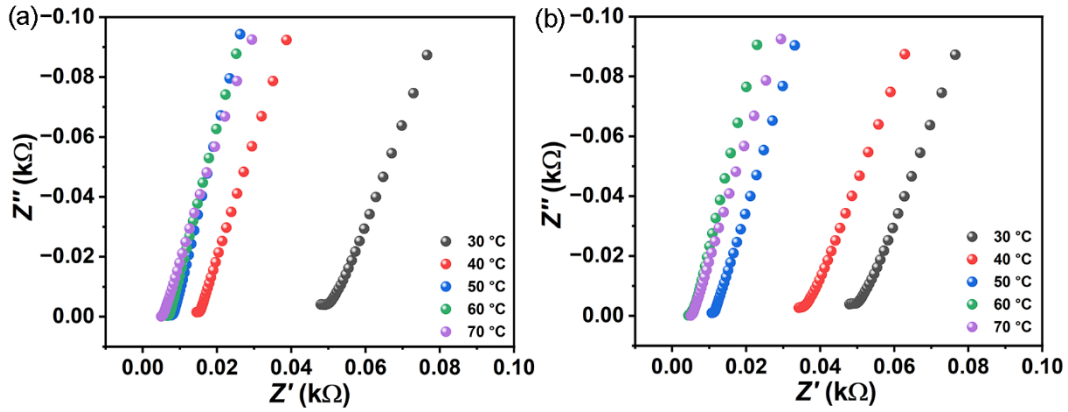

Fig. S37. Nyquist plots for the heating-cooling cycle of UiO-66-2COOH aerogel at 98% RH: (a) the heating cycle (30 to 70 ℃); (b) the cooling cycle (70 to 30 ℃).

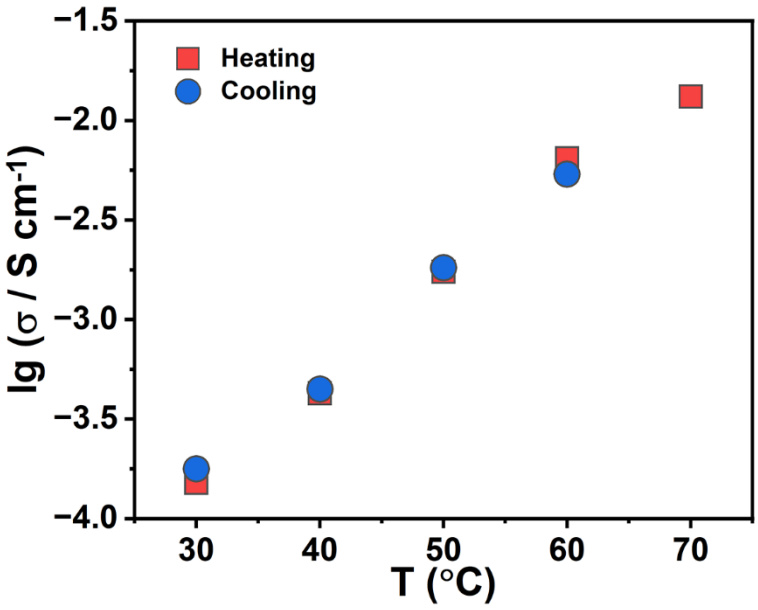

Fig. S38. Proton conductivities for the heating-cooling cycle of UiO-66-COOH aerogel at 98% RH.

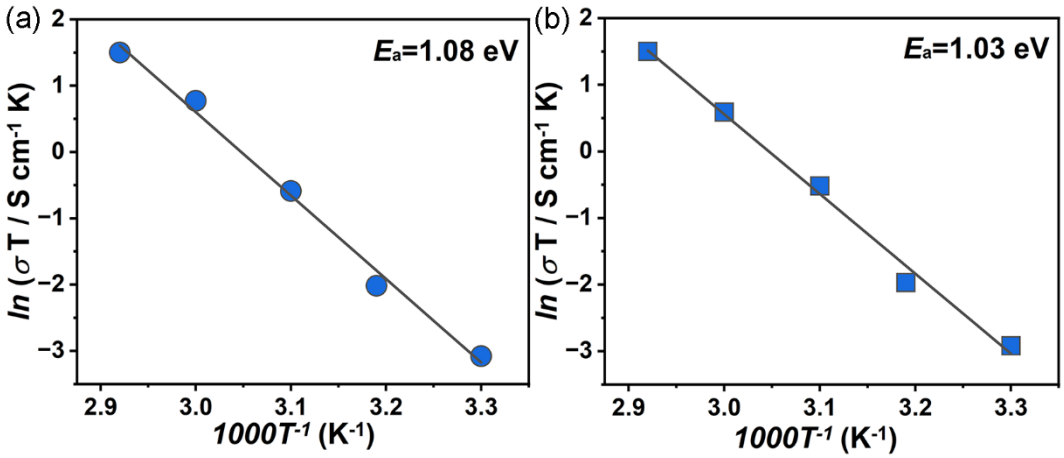

Fig. S39. Arrhenius plots of UiO-66-COOH aerogel for every heating-cooling cycle at the temperature range of 30 to 70 ℃ and 98% RH: (a) the heating cycle (30 to 70 ℃); (b) the cooling cycle (70 to 30 ℃).

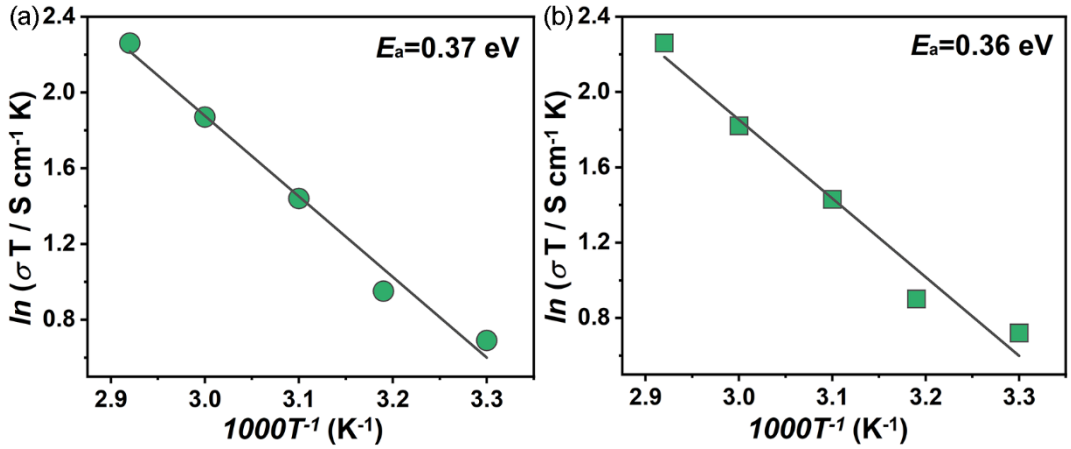

Fig. S40. Arrhenius plots of UiO-66-2COOH aerogel for every heating-cooling cycle at the temperature range of 30 to 70 ℃ and 98% RH: (a) the heating cycle (30 to 70 ℃); (b) the cooling cycle (70 to 30 ℃).

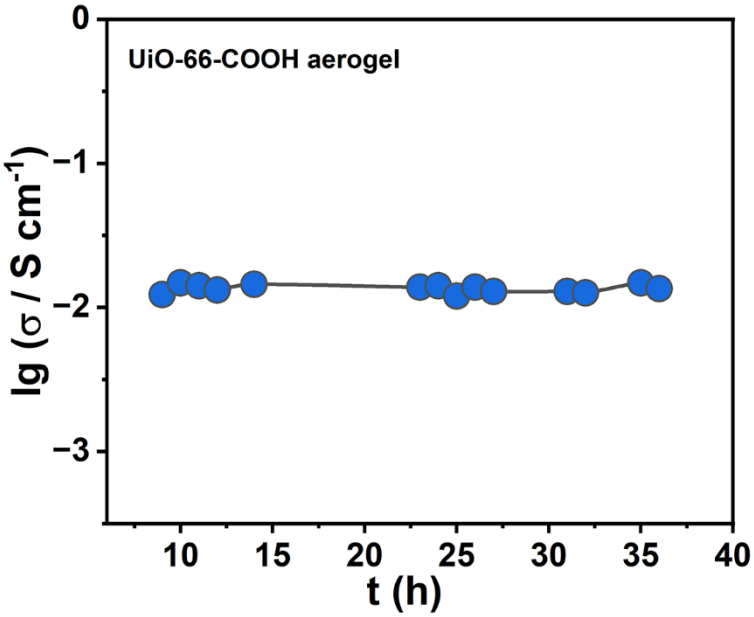

Fig. S41. The time-dependent proton conductivities of UiO-66-COOH aerogel measured at 70 ℃ and 98% RH.

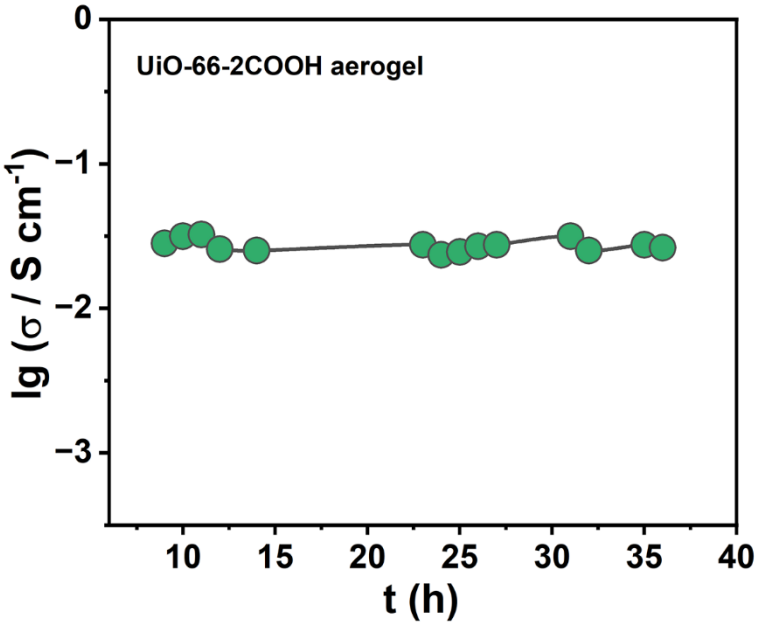

Fig. S42. The time-dependent proton conductivities of UiO-66-2COOH aerogel measured at 70 ℃ and 98% RH.

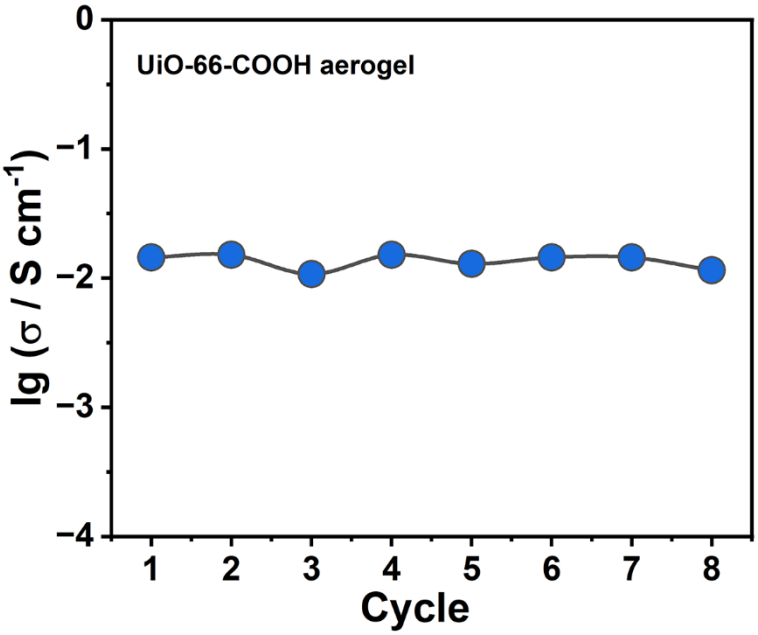

Fig. S43. The cycle-dependent proton conductivities of UiO-66-COOH aerogel measured at 70 ℃ and 98% RH.

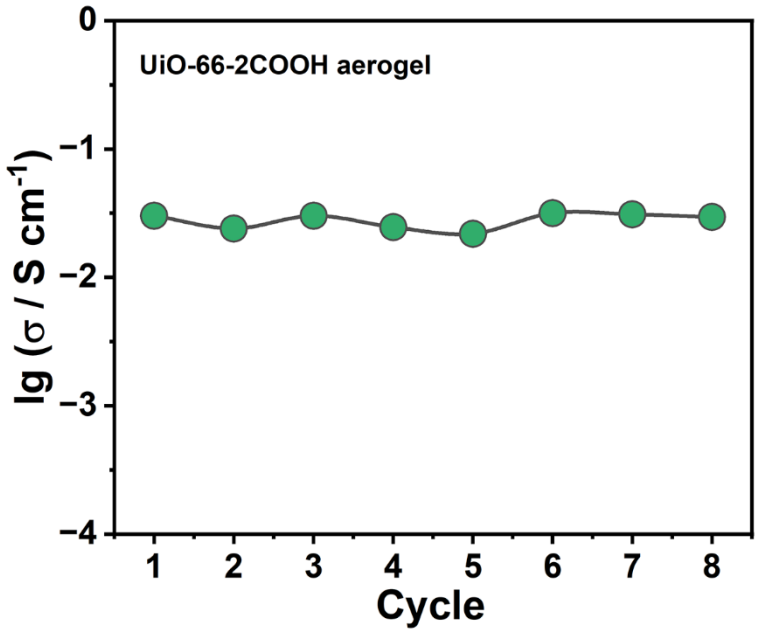

Fig. S44. The cycle-dependent proton conductivities of UiO-66-2COOH aerogel measured at 70 ℃ and 98% RH.

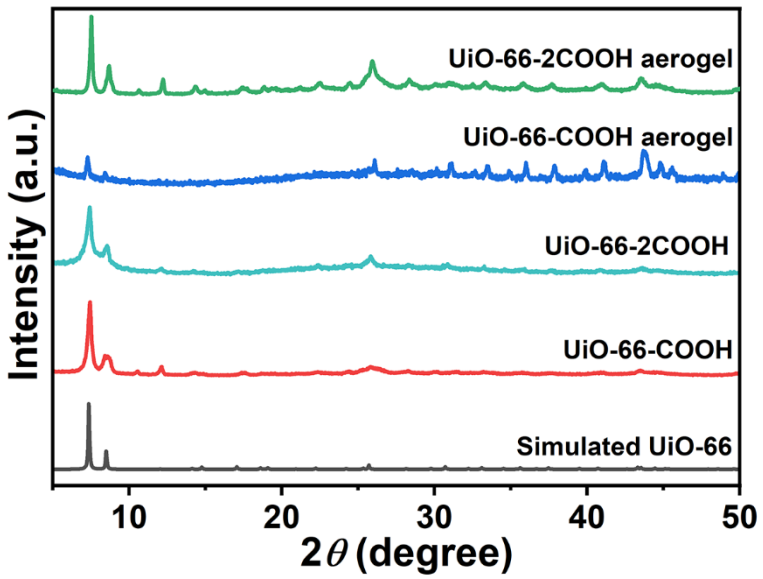

Fig. S45. XRD patterns of simulated UiO-66, UiO-66-COOH, UiO-66-2COOH, UiO-66-COOH aerogel, and UiO-66-2COOH aerogel undergoing proton conduction measurements.

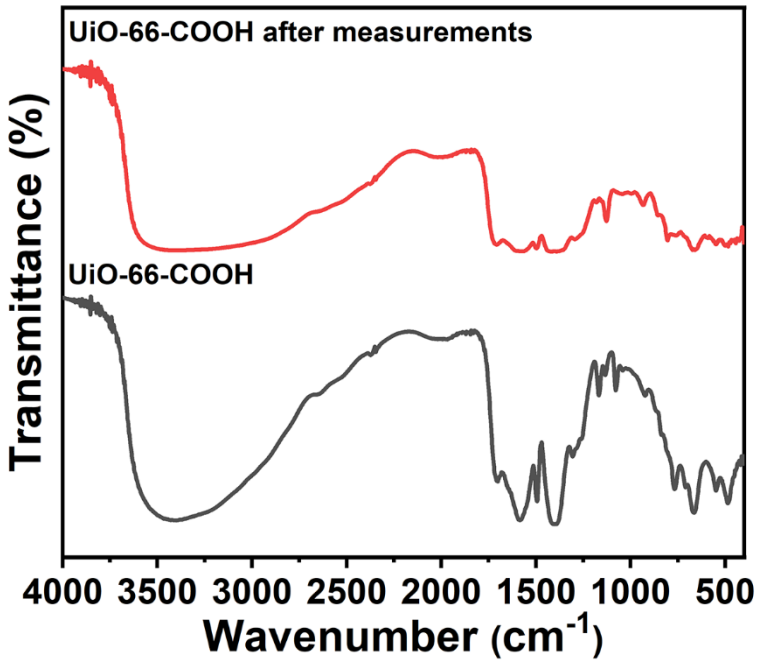

Fig. S46. FT-IR spectra of as-synthesized UiO-66-COOH and UiO-66-COOH undergoing proton conduction measurements.

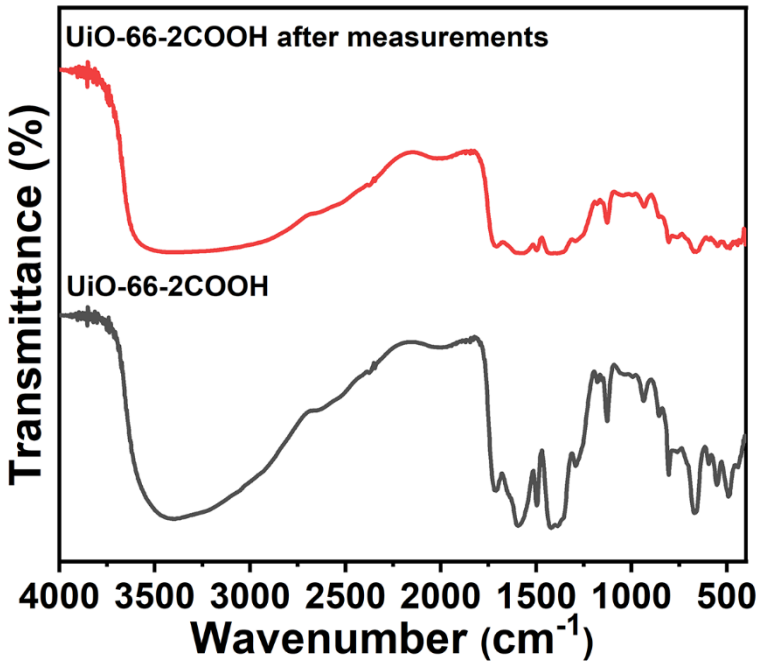

Fig. S47. FT-IR spectra of as-synthesized UiO-66-2COOH and UiO-66-2COOH undergoing proton conduction measurements.

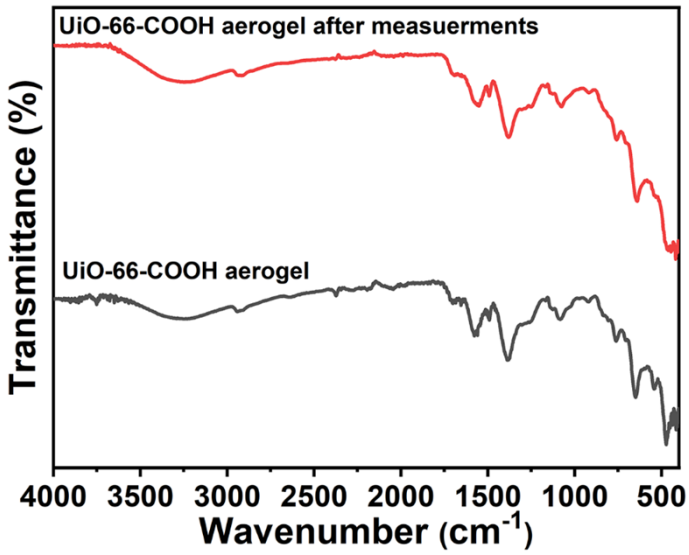

Fig. S48. FT-IR spectra of as-synthesized UiO-66-COOH aerogel and UiO-66-COOH aerogel undergoing proton conduction measurements.

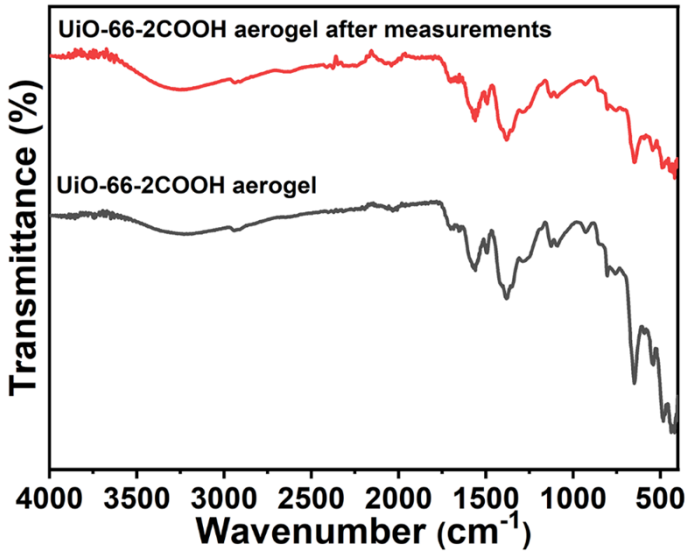

Fig. S49. FT-IR spectra of as-synthesized UiO-66-2COOH aerogel and UiO-66-2COOH aerogel undergoing proton conduction measurements.

References

1 N. Zhang, L.-Y. Yuan, W.-L. Guo, S.-Z. Luo, Z.-F. Chai and W.-Q. Shi, *ACS Appl. Materi. Interfaces,* 2017, **9**, 25216-25224.

2 Q. Zhang, D. Li, J. Wang, S. Guo, W. Zhang, D. Chen, Q. Li, X. Rui, L. Gan and S. Huang, *Nanoscale* 2020, **12**, 6976-6982.